The dynamical effects of the bar on the Galactic thin and thick disks

Monari, Giacomo

Chapter 3

3D test particle simulations of the Galactic disks II. The effects of the bar in frequency space.

Based on Monari, Helmi & Antoja (2014).
In preparation.

Abstract

The Galactic bar can be described as a small perturbation onto the axisymmetric potential that represents most of the mass in the Milky Way. With the help of Perturbation Theory we define resonant trapping and study the regions of velocity space occupied by trapped orbits for a simple 2D model of the Milky Way. Then we extend our analysis to the 3D simulations presented in Chapter 2, using Fourier frequency analysis to classify orbits trapped to resonances and to identify irregular orbits. For our default bar model, we find that roughly 16% of orbits are trapped to resonances in our simulations and that they create features in the velocity distribution. The fraction of orbits trapped to horizontal ($\Omega_R : \Omega_\phi = n : m$) resonances and their characteristics do not depend on height from the Galactic plane but rather on the angle from the bar and distance from the Galactic center. The fraction of orbits trapped to the vertical resonances ($\Omega_R : \Omega_z = n : m$, $\Omega_\phi : \Omega_z = n' : m'$) instead grows as the height increases. We explore two additional bar models and find that the main difference resides in the number of trapped and irregular orbits, and this is directly related to the strength of the perturbation.

3.1 Introduction

The problem of understanding the effects of non-axisymmetric perturbations like the Galactic bar or spiral arms on the dynamics of stars in the Milky Way (or in other galaxies) has been studied on numerous occasions. Through resonant effects the bar and spiral arms can modify significantly the phase-space distribution of the stars in galaxies. This leads to the expectation that there is a one-to-one relationship between these effects and the characteristics of the perturbation, as if phase-space would have a characteristic signature of the bar or the spiral arms near the resonances. Therefore, by studying the phase-space distribution of stars even far from the perturbation, we can know its parameters (e.g., pattern speed, mass, geometry), as well as obtain information about the characteristic parameters of the Galaxy as a whole (e.g., its circular speed curve).

The first works on this subject were mostly analytical. In a series of papers from the '70s - '80s (Contopoulos 1975; Contopoulos & Mertzanides 1977; Contopoulos 1979; Contopoulos & Papayannopoulos 1980; Contopoulos 1981; Contopoulos & Grosbol 1986) 2D perturbation theory models were used. These authors studied the orbits induced by some simple bar or spiral arm potentials rotating with a constant pattern speed, and introduced a terminology to classify the periodic orbits (x_i orbits) that is still widely used. Contopoulos (1979) also studied the *density* response of the stars in a galaxy near the Inner Lindblad Resonance associated to a spiral pattern. Along similar lines, using also 2D perturbation theory, Weinberg (1994) studied the *kinematic* response (mean velocity and dispersion) of the Galactic disk, near Corotation, Inner and Outer Lindblad resonances to a bar perturbation with variable pattern speed. Kuijken & Tremaine (1991) studied the kinematic response of a disk to a more general class of perturbations, as function of the angle from the perturbation. Finally, Kalnajs (1991) proposed that the different orbital families induced by the bar could create distinctive signatures in the kinematics of the stars in the Solar Neighborhood.

A big impulse to the topic came from the systematic exploration of the kinematics of stars in the Solar Neighborhood, after the launch of the *Hipparcos* mission. The Solar Neighborhood was found to be rich in substructures (Dehnen 1998), composed by stars that not always had the same age and chemical composition (Famaey et al. 2005). Therefore it was believed that many of them could have their origin in the resonant effects of the bar or the spiral arms, as in Kalnajs (1991) hypothesis.

Since *Hipparcos*, and with the advances in computational power, different authors tried to fit the observed kinematics with numerical simulations of the Milky Way using models including the bar (Dehnen 2000; Fux 2001), the spiral arms (De Simone et al. 2004; Antoja et al. 2011), or both (Antoja et al. 2009; Quillen et al. 2011). Further insights from analytic models were obtained by, e.g., Quillen (2003) who studied the chaos in the Solar Neighborhood due to overlap between the bar and the spiral arms resonances. Sellwood (2010) studied the distribution of stars of the *Geneva-Copenhagen* survey in the angle coordinates of a spherical 2D model and McMillan (2011, 2013) tried to fit an analytical distribution function composed by an axisymmetric phase-mixed part and a non-mixed resonant term due to a spiral perturbation to the *RAVE* observations, in order to explain the Hyades moving group.

This Chapter complements the study presented in Chapter 2 on the effects of the bar on the Galactic disk. We focus here on the resonant trapping induced by the bar, and the relation to the local kinematic structures present in the velocity distribution. We

first approach this problem with the help of perturbation theory for a simple 2D model of the Galaxy, in order to define the resonant trapping and get insight into the dynamics. Then we turn to our 3D test particle simulations. We perform a Fourier analysis of the orbits of stars across the whole disk. This allows to quantify the presence of resonances also far from the Galactic plane as well as to test the validity of the 2D analytic model.

In Sect. 3.2 we describe the dynamics of the problem using the Perturbation Theory in 2D and we predict the location of the orbits trapped to the resonances at different positions in the Galactic disk. In Sect. 3.3 we explain the Fourier transform method used to obtain the orbits' frequencies in our numerical experiments. In Sect. 3.4 we present the results obtained with the frequency analysis and in Sect. 3.5 we conclude.

3.2 Dynamics near the resonances

3.2.1 Generalities

The Milky Way contains a bar and spiral arms. Their gravitational potential can be described as a small perturbation onto an axisymmetric background, i.e, $\Phi(R,z) = \Phi_0(R,z) + \Phi_\mathrm{b}(R,\phi,z)$, where (R,ϕ,z) are the usual cylindrical coordinates and Φ_b is the perturbation. We can write the Hamiltonian of the problem as

$$H\left(\boldsymbol{J}\right) = H_0\left(\boldsymbol{J}\right) + \delta H(\boldsymbol{J},\boldsymbol{\theta}), \tag{3.1}$$

where H_0 is the term governing the dynamics in the unperturbed background potential (that we assume to be integrable), $\delta H = \Phi_\mathrm{b}$ the perturbation, and $(\boldsymbol{J},\boldsymbol{\theta})$ a set of actions and angles for H_0. The angles $\boldsymbol{\theta}$ evolve in H_0 with frequencies $\boldsymbol{\Omega} = \partial H_0/\partial \boldsymbol{J}$. The resonances are defined using the frequencies as

$$\mathbf{l}\cdot\boldsymbol{\Omega} = 0, \tag{3.2}$$

where $\mathbf{l}$ is a vector of integers.

Near a resonance, like that described by Eq. (3.2), we can define a new set of angle-action coordinates more appropriate for the study of the perturbed problem. This, in N dimensions, is done via the canonical transformation $(\boldsymbol{J},\boldsymbol{\theta}) = (\{J_1,...,J_N\},\{\theta_1,...,\theta_N\}) \rightarrow (\boldsymbol{I},\boldsymbol{\phi}) = (\{I_\mathrm{s},I_\mathrm{f1},...,I_{\mathrm{f},N-1}\},\{\phi_\mathrm{s},\phi_\mathrm{f1},...,\phi_{\mathrm{f},N-1}\})$,

$$\begin{array}{ll}
\phi_\mathrm{s} = \mathbf{l}\cdot\boldsymbol{\theta}, & J_1 = l_1 I_\mathrm{s} + I_\mathrm{f1} \\
\phi_\mathrm{f1} = \theta_1, & J_2 = l_2 I_\mathrm{s} + I_\mathrm{f2} \\
... & \\
\phi_{\mathrm{f},N-2} = \theta_{N-2}, & J_{N-1} = l_{N-1} I_\mathrm{s} + I_{\mathrm{f},N-1} \\
\phi_{\mathrm{f},N-1} = \theta_{N-1}, & J_N = l_N I_\mathrm{s}.
\end{array} \tag{3.3}$$

The angle ϕ_s is called "slow angle", because near the resonance it evolves at a frequency $\Omega_\mathrm{s} = \mathbf{l}\cdot\boldsymbol{\Omega} \approx 0$.

It can be shown (Kaasalainen 1994; Binney & Tremaine 2008, see also Eq. (3.24b) below) that near to the resonance the equation of motion of ϕ_s is approximately that of a pendulum. The energy of the pendulum is

$$E_\mathrm{p} = \frac{1}{2}\dot{\phi_\mathrm{s}}^2 + V_\mathbf{l}(\phi_\mathrm{s}), \tag{3.4}$$

where the potential $V_{\rm l}(\phi_{\rm s})$ is different for each resonance. If $E_{\rm p} \geq \max(V_{\rm l})$ then $\phi_{\rm s}$ circulates (i.e., it always increases with time), else $\phi_{\rm s}$ librates (i.e., it oscillates between two values). In this latter case the orbit is said to be "trapped to the resonance".

3.2.2 Perturbation theory: a simple case

In this Section we apply the formalism just introduced to a very simple case, to get insight into the dynamics induced by the bar as it perturbs the motions of stars in the Galactic disk.

Following Weinberg (1994), we study the problem in two dimensions, assuming that the background potential corresponds to that of a galaxy with a flat rotation curve with circular speed v_0,

$$\Phi_0(R) = v_0^2 \ln\left(\frac{R}{R_0}\right). \tag{3.5}$$

We assume that the bar perturbation rotates with constant pattern speed $\Omega_{\rm b}$ and to be a pure quadrupole, i.e.,

$$\Phi_{\rm b}(R,\phi) = {\rm Re}\left\{U_2(R){\rm e}^{i2(\phi-\Omega_{\rm b}t)}\right\}, \tag{3.6}$$

where

$$U_2(R) = -\epsilon v_0^2 \begin{cases} (R/r_{\rm b})^2 & \text{if } R < r_{\rm b} \\ (R/r_{\rm b})^{-3} & \text{if } R \geq r_{\rm b}. \end{cases} \tag{3.7}$$

Here (R,ϕ) are polar coordinates, with ϕ measured from the long axis of the bar, $r_{\rm b}$ is the dimension of the bar and ϵ denotes the amplitude of the perturbation compared to the background potential, which itself is proportional to v_0^2 (see Eq. 3.5).

We study the problem in the epicyclic approximation (Binney & Tremaine 2008) i.e., we assume that the orbits of stars in the disk are not too eccentric. In this case Eq. (3.1) reads

$$H = H_0\left(J_R, J_\phi\right) - \Omega_{\rm b} J_\phi + \delta H\left(J_R, J_\phi, \theta_R, \theta_\phi\right). \tag{3.8}$$

H is often referred to as "Jacobi Integral" and H_0 is the Hamiltonian of the potential responsible for the flat rotation curve. The coordinates $(J_R, J_\phi, \theta_R, \theta_\phi)$ are action angle coordinates in the unperturbed Hamiltonian. In particular J_ϕ is the angular momentum. The angular frequencies are

$$\dot{\theta}_R = \kappa, \quad \dot{\theta}_\phi = \Omega, \tag{3.9}$$

where $\kappa(R)$ and $\Omega(R)$ are the epicyclic and circular frequency respectively[1]. The effective background Hamiltonian is in this case $H_0^{\rm eff}\left(J_R, J_\phi\right) \equiv H_0\left(J_R, J_\phi\right) - \Omega_{\rm b} J_\phi$, and Eq. (3.2) can be expressed as

$$l_R \kappa + l_\phi\left(\Omega - \Omega_{\rm b}\right) = 0, \tag{3.10}$$

where l_R and l_ϕ are integers. The canonical transformation given by Eq. (3.3), becomes

$$\begin{array}{ll} \phi_{\rm s} = l_R\theta_R + l_\phi\left(\theta_\phi - \Omega_{\rm b}t\right), & J_R = l_R I_{\rm s} + I_{\rm f}, \\ \phi_{\rm f} = \theta_R, & J_\phi = l_\phi I_{\rm s}. \end{array} \tag{3.11}$$

[1] We consider here Lindblad's version of the epicyclic theory, used also in Lynden-Bell & Kalnajs (1972) and Weinberg (1994). In this version the $(J_R, J_\phi, \theta_R, \theta_\phi)$ coordinates are not canonical. To make them canonical (and obtain a more accurate representation of the orbits) one should use $\dot{\theta}_\phi = \Omega + \frac{{\rm d}\kappa}{{\rm d}J_\phi}$ and add a (small) term $\propto \sin 2\theta_R$ to $f(\theta_R)$ in Eq. (3.15) (Dehnen 1999).

The perturbation δH is cyclic in the $(\phi_\mathrm{s}, \phi_\mathrm{f})$ angles (as these are combinations of the (θ_ϕ, θ_R) angles) so δH can be expanded in a Fourier series as

$$\delta H = \Phi_\mathrm{b} = \mathrm{Re}\left\{\sum_{j=-\infty}^{\infty}\sum_{k=-\infty}^{\infty} h_{jk}(I_\mathrm{s}, I_\mathrm{f}) \exp\left[i(j\phi_\mathrm{f} + k\phi_\mathrm{s})\right]\right\}. \tag{3.12}$$

At this point we argue that any term in the sum that contains ϕ_f has a negligible effect on the dynamics: these terms give rise to forces that rapidly average to zero (Binney & Tremaine 2008). We therefore drop all the terms in the j-sum in Eq. (3.12), except $j = 0$. Therefore,

$$\delta H = \mathrm{Re}\left\{U_2(R)\mathrm{e}^{i2(\phi-\Omega_\mathrm{b}t)}\right\} \approx \mathrm{Re}\left\{\sum_{k=-\infty}^{\infty} h_k(I_\mathrm{s}, I_\mathrm{f})\mathrm{e}^{ik\phi_\mathrm{s}}\right\}, \tag{3.13}$$

where

$$h_k \equiv h_{0k} = \frac{1}{(2\pi)^2}\int_0^{2\pi}\int_0^{2\pi} \mathrm{d}\phi_\mathrm{f}\mathrm{d}\phi_\mathrm{s} U_2(R)\mathrm{e}^{i2(\phi-\Omega_\mathrm{b}t)}\mathrm{e}^{-ik\phi_\mathrm{s}}. \tag{3.14}$$

To estimate h_k we write the deviation of the azimuthal position of the star ϕ from its guiding center θ_ϕ, as

$$f(\theta_R) \equiv \theta_\phi - \phi. \tag{3.15}$$

In the epicyclic approximation

$$f(\theta_R) = -\frac{\Omega(R_\mathrm{g})}{\kappa(R_\mathrm{g})}\frac{2a}{R_\mathrm{g}}\sin\theta_R, \tag{3.16}$$

where $R_\mathrm{g} = J_\phi/v_0$ is the guiding center radius and a is the amplitude of the epicyclic motion. From Eq. (3.11), $\theta_\phi = \phi_\mathrm{s}/l_\phi - l_R\theta_R/l_\phi + \Omega_\mathrm{b}t$, $\phi_\mathrm{f} = \theta_R$, and therefore

$$\begin{aligned} h_k &= \frac{1}{(2\pi)^2}\int_0^{2\pi}\int_0^{2\pi} \mathrm{d}\theta_R\mathrm{d}\phi_\mathrm{s} U_2(R)\mathrm{e}^{i2\left[\frac{\phi_\mathrm{s}}{l_\phi} - \frac{l_R}{l_\phi}\theta_R - f(\theta_R)\right]}\mathrm{e}^{-ik\phi_\mathrm{s}} = \\ &= \frac{c_2(l_\phi, k)}{(2\pi)^2}\int_0^{2\pi}\mathrm{d}\theta_R U_2(R)\mathrm{e}^{-i2\left[\frac{l_R}{l_\phi}\theta_R + f(\theta_R)\right]}, \end{aligned} \tag{3.17}$$

where

$$c_2(l_\phi, k) = \begin{cases} \frac{\mathrm{e}^{i\left(\frac{2}{l_\phi}-k\right)2\pi}-1}{i\left(\frac{2}{l_\phi}-k\right)} & \text{if } kl_\phi \neq 2 \\ 2\pi & \text{if } kl_\phi = 2. \end{cases} \tag{3.18}$$

If $l_\phi \leq 2$, $c_2(l_\phi, k) = \delta_{2,l_\phi k}$. The integrand in Eq. (3.17) is an even function of θ_R, therefore

$$h_k = \frac{c_2(l_\phi, k)}{2\pi^2}\int_0^{\pi}\mathrm{d}\theta_R U_2(R)\cos\left\{2\left[\frac{l_R}{l_\phi}\theta_R + f(\theta_R)\right]\right\}. \tag{3.19}$$

Using the perturbed slow and fast actions we can re-write Eq. (3.8) as

$$H = H_0(I_\mathrm{s}, I_\mathrm{f}) - l_\phi\Omega_\mathrm{b}I_\mathrm{s} + \mathrm{Re}\left\{\sum_{k=-\infty}^{\infty} h_k\mathrm{e}^{ik\phi_\mathrm{s}}\right\}. \tag{3.20}$$

If we expand the effective background Hamiltonian $H_0^{\rm eff} = H_0 - l_\phi \Omega_{\rm b} I_{\rm s}$ around the value of $I_{\rm s}$ at the resonance we obtain

$$H_0^{\rm eff} \approx H_0^{\rm eff}(I_{\rm f}, I_{\rm s,res}) + \frac{\partial H_0^{\rm eff}}{\partial I_{\rm s}}\Big|_{\rm res}(I_{\rm s} - I_{\rm s,res}) + \frac{1}{2}\frac{\partial^2 H_0^{\rm eff}}{\partial I_{\rm s}^2}\Big|_{\rm res}(I_{\rm s} - I_{\rm s,res})^2 . \tag{3.21}$$

The second term in this expansion is null because $\partial H_0^{\rm eff}/\partial I_{\rm s} = \Omega_{\rm s}$, which is exactly zero at the resonance. At this point we assume $I_{\rm f}$ constant, as its evolution is adiabatic. The effective one-dimensional Hamiltonian that governs the motion in the $(I_{\rm s}, \phi_{\rm s})$ plane then becomes

$$\hat{H} = \frac{1}{2}\frac{\partial \Omega_{\rm s}}{\partial I_{\rm s}}\Big|_{\rm res}(I_{\rm s} - I_{\rm s,res})^2 + {\rm Re}\left\{\sum_{k=-\infty}^{\infty} h_k {\rm e}^{ik\phi_{\rm s}}\right\}. \tag{3.22}$$

Hamilton's equations in this case read

$$\dot{I}_{\rm s} = {\rm Re}\left\{ i \sum_{k=-\infty}^{\infty} k h_k(I_{\rm s}) {\rm e}^{ik\phi_{\rm s}}\right\}, \tag{3.23a}$$

$$\dot{\phi}_{\rm s} = \frac{\partial \Omega_{\rm s}}{\partial I_{\rm s}}\Big|_{\rm res}(I_{\rm s} - I_{\rm s,res}) + {\rm Re}\left\{\frac{\partial h_k}{\partial I_{\rm s}} {\rm e}^{ik\phi_{\rm s}}\right\}, \tag{3.23b}$$

and

$$\ddot{\phi}_{\rm s} \approx \frac{\partial \Omega_{\rm s}}{\partial I_{\rm s}}\Big|_{\rm res}\dot{I}_{\rm s}, \tag{3.24a}$$

$$\ddot{\phi}_{\rm s} \approx \frac{\partial \Omega_{\rm s}}{\partial I_{\rm s}}\Big|_{\rm res}{\rm Re}\left\{ i \sum_{k=-\infty}^{\infty} k h_k(I_{\rm s}) {\rm e}^{ik\phi_{\rm s}}\right\}, \tag{3.24b}$$

where in the last equation we have neglected the terms proportional to powers of ϵ larger or equal than 2 (recall that $h_k \propto \epsilon$). Eq. (3.24b) is the pendulum equation that governs the motion of the slow angle $\phi_{\rm s}$. In this case

$$V(\phi_{\rm s}) = {\rm Re}\left\{\sum_{k=-\infty}^{\infty} \frac{\partial \Omega_{\rm s}}{\partial I_{\rm s}} h_k {\rm e}^{ik\phi_{\rm s}}\right\}. \tag{3.25}$$

The angle $\phi_{\rm s}$ represents the precession of the orbit i.e., it describes the angle from the long axis of the bar recorded at the apocenters (relative maxima in R). A trapped orbit precesses back and forward between two values of $\phi_{\rm s}$. Integrating Eq. (3.24a) with respect to the time variable t, we find

$$I_{\rm s}(t) = I_{\rm s}(0) + \left(\frac{\partial \Omega_{\rm s}}{\partial I_{\rm s}}\Big|_{\rm res}\right)^{-1}\left[\dot{\phi}_{\rm s}(t) - \dot{\phi}_{\rm s}(0)\right], \tag{3.26}$$

and, since $I_{\rm s} = R^2\dot{\phi}/l_\phi$, then

$$R^2(t) = \frac{1}{\dot{\phi}(t)}\left\{ J_\phi(0) + l_\phi\left(\frac{\partial \Omega_{\rm s}}{\partial I_{\rm s}}\Big|_{\rm res}\right)^{-1}\left[\dot{\phi}_{\rm s}(t) - \dot{\phi}_{\rm s}(0)\right]\right\}. \tag{3.27}$$

From Eq. (3.11) and Eq. (3.15) we see that

$$\dot{\phi} = \dot{\phi}_{\rm ep}(\theta_R) + \Delta\dot{\phi}(\phi_{\rm s}), \tag{3.28}$$

Table 3.1: Color coding of orbits trapped to the resonances in the plots of this work, defined by the indices l_R, l_ϕ and l_z.

(l_R, l_ϕ, l_z)	Color
$(1, 1, 0)$	Yellow
$(1, 2, 0)$	Red
$(1, 3, 0)$	Purple
$(1, 4, 0)$	Blue
$(3, 0, 2)$	Light green
$(1, 0, 1)$	Orange
$(1, 0, 2)$	Dark green
$(0, 1, 1)$	Gray
All	Black
Irregular	Light blue

where we have defined $\dot{\phi}_{\rm ep} \equiv \Omega - f'(\theta_R)\kappa$ (the value of $\dot{\phi}$ without the bar perturbation in the epicyclic approximation) and $\Delta\dot{\phi} \equiv \dot{\phi}_{\rm s}/l_\phi - l_R\kappa/l_\phi + \Omega_{\rm b} - \Omega$. Since $\dot{\phi}_{\rm ep} \gg \Delta\dot{\phi}$

$$\begin{aligned} R^2 &\approx \frac{J_\phi(0)}{\dot{\phi}_{\rm ep}(\theta_R)} - l_\phi \left(\frac{\partial \Omega_{\rm s}}{\partial I_{\rm s}}\Big|_{\rm res} \right)^{-1} \frac{\dot{\phi}_{\rm s}(t) - \dot{\phi}_{\rm s}(0)}{\dot{\phi}_{\rm ep}(\theta_R)} = \\ &= \frac{J_\phi(0)}{\dot{\phi}_{\rm ep}(\theta_R)} - l_\phi \left(\frac{\partial \Omega_{\rm s}}{\partial I_{\rm s}}\Big|_{\rm res} \right)^{-1} \frac{\sqrt{E_{\rm p} - V(\phi_{\rm s})} - \dot{\phi}_{\rm s}(0)}{\dot{\phi}_{\rm ep}(\theta_R)}. \end{aligned} \tag{3.29}$$

From Eq. (3.29) we see that the motion in R is composed by an "epicyclic" unperturbed part, dependent only on θ_R and a part depending also on the $\phi_{\rm s}$ angle. Hence, R is the combination of two periodic motions. Depending on the value of $\phi_{\rm s}$, the orbit will be more or less elongated in the R direction. In particular, for orbits with guiding center radius $R_{\rm g}$ inside the Outer Lindblad Resonance (OLR, $l_R = 1$, $l_\phi = 2$), the orbits are most elongated in R when $\phi_{\rm s} = \pm\pi/2$ and for orbits outside the OLR at $\phi_{\rm s} = 0$ (see Fig. 3.1 and Weinberg 1994).

3.2.3 Resonances and velocity space

In Fig. 3.2 we assume $v_0 = 220$ km s^{-1}, $\Omega_{\rm b} = 50$ km s^{-1} kpc^{-1}, $r_{\rm b} = 3.5$ kpc and $\epsilon = 0.05,\ 0.1$, and we compute $E_{\rm p} - \max(V)$ for orbits passing through the given (R, ϕ) locations with velocities $(v_R, v_\phi) = (-\dot{R}, R\dot{\phi})$. The contours represent $E_{\rm p} - \max(V) = 0$ for different combinations of (l_R, l_ϕ) (see Table 3.1 for the color coding). Orbits inside these contours are, according to the perturbation theory, trapped to the corresponding resonance. We see how these contours enclose regions that look like islands in the (v_R, v_ϕ) space.

In the top left panel of Fig. 3.2 we have assumed $(R, \phi) = (8\ {\rm kpc}, -20^\circ)$ while in the top right plot we assume $(R, \phi) = (8\ {\rm kpc}, 0)$ for $\epsilon = 0.05$. From the comparison of these two plots we see how the angle from the bar ϕ affects the location of the islands. In particular, at $\phi = 0$ the islands are completely symmetric with the respect to the $v_R = 0$ axis, while at $(R, \phi) = (8\ {\rm kpc}, -20^\circ)$ they are asymmetric. Let us for example consider

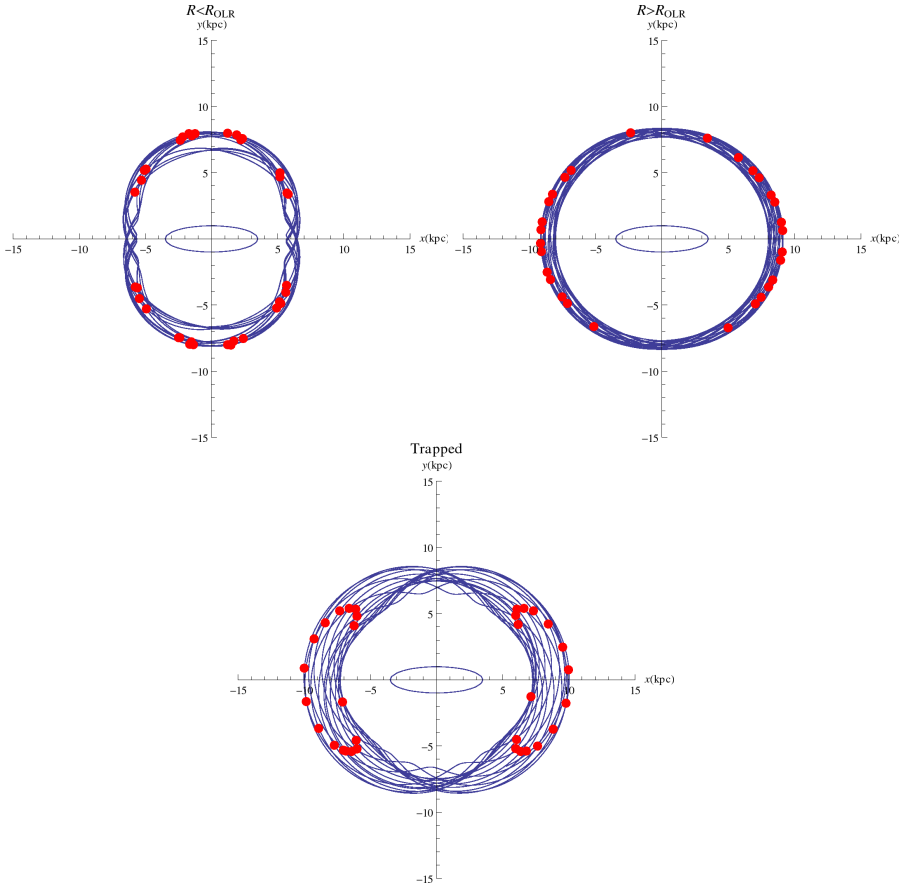

Figure 3.1: Orbits integrated in the potential $\Phi_0 + \Phi_b$ given by Eqs. (3.5)-(3.7) for $t \approx 1$ Gyr and in the frame of reference corotating with the bar. The red dots correspond to the position of the apocenters, the local maxima of $R(t)$. The ellipse in the center of the plot represents the bar. Top: examples of orbits not trapped to a resonance for $R_g < R_{OLR}$ (left) and $R_g > R_{OLR}$ (right). Bottom: an orbit trapped to the $(l_R, l_\phi) = (1, 2)$ (OLR) resonance. The azimuth ϕ of the apocenters is equivalent to the slow angle ϕ_s. In the non-trapped cases the apocenter circulates around the center, while in the trapped case it oscillates between two angles. Moreover, in the non-trapped cases R at the apocenters is maximum at $\phi_s = 0$ ($\phi_s = \pm 90°$) for $R_g > R_{OLR}$ ($R_g < R_{OLR}$). For the trapped orbits R at the apocenters is maximum and minimum at $\phi_s = 0$.

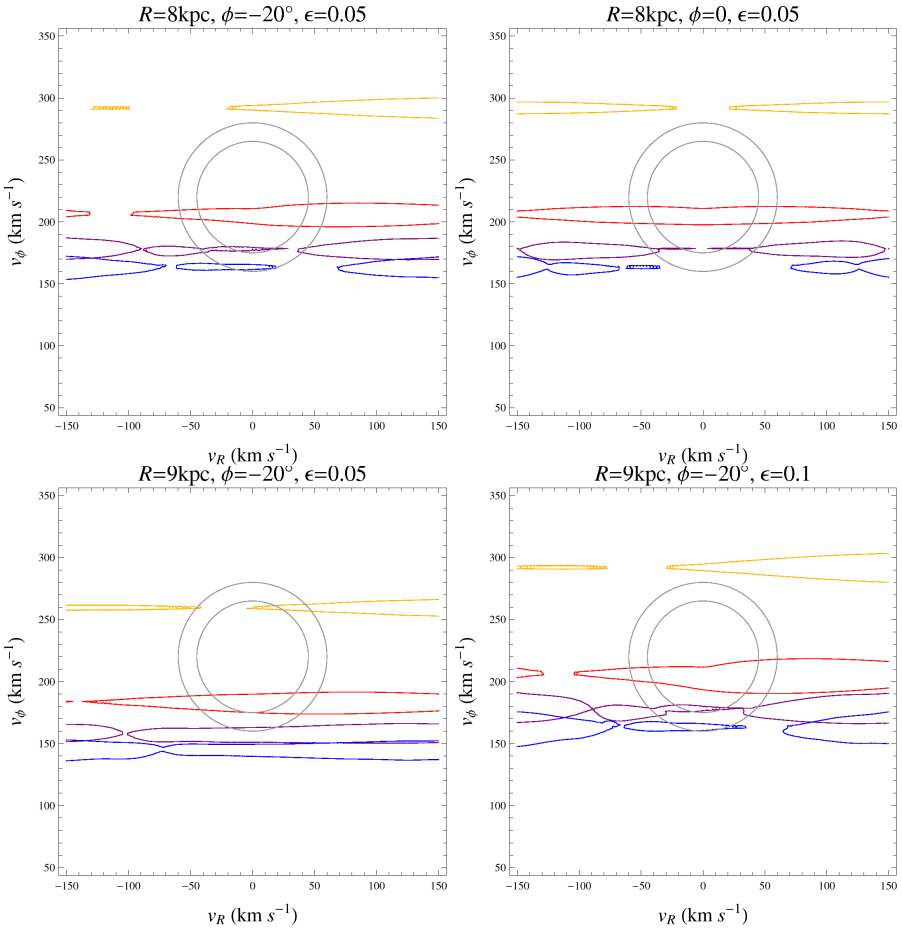

Figure 3.2: Predictions of the perturbation theory presented in Sect. 3.2.2 for different (R, ϕ) and ϵ on v_R vs. v_ϕ, for a simple Galaxy model, with $\Omega_b = 50$ km s^{-1} kpc^{-1}. The contours enclose the regions of resonant trapping, estimated from Eqs. (3.23b)-(3.25) neglecting the terms in the sums with $|k| > 10$. The color coding is given in Table 3.1. The gray circles are centered at $(v_R, v_\phi) = (0, 220$ km s$^{-1})$ and have radius 45 and 60 km s^{-1} respectively and roughly indicate the 1σ extension in velocity space of the thin and thick disks in the Solar Neighborhood.

the contours of the $(l_R, l_\phi) = (1, 2)$ (red) resonance. For $\phi = 0$ the island represents orbits trapped to the resonance and arriving at $(R, \phi) = (8 \text{ kpc}, 0)$ moving outwards ($v_R < 0$) or inwards ($v_R > 0$). At $\phi = -20°$ the islands are asymmetric. If we consider a gaussian distribution of stars to represent the thin or the thick disk (the gray circles in figure are meant to represent the 1σ contours of these disks), we see that the majority of stars crosses this point moving inwards in the Galaxy.

If instead we change R, and we focus on e.g., $(R, \phi) = (9 \text{ kpc}, -20°)$ (Fig. 3.2, bottom right), the regions where the orbits are trapped shift to lower v_ϕ. Vice versa, moving inwards in R would shift the contours to higher v_ϕ. The symmetry of some resonant families with respect to v_R is also changed (see especially the $(1, 3)$ and $(1, 4)$ resonances in the figure).

Finally, increasing the bar strength to $\epsilon = 0.1$ (Fig. 3.2, bottom left) we see that the contours become wider in v_ϕ, at a fixed v_R. This is due to the fact that a stronger bar increases the volume of the phase-space where resonant trapping is possible.

Fig 3.2 shows that in some cases the contours overlap. In the regions where the contours overlap, the perturbation analysis performed fails to predict to which resonance the orbits are trapped. This happens because this approximation treats each resonance separately. In other words, it can happen that according to the perturbation analysis an orbit can be trapped to more than one resonance. We remind the reader that the phase-space regions of transition between different kinds of resonant trapping correspond usually with regions of chaotic orbits (a phenomenon also known as *resonance overlap*, see Binney & Tremaine 2008).

3.3 Fourier analysis

The perturbation theory described in Sect. 3.2, has the disadvantage that it cannot be easily extended to more complicated systems. In particular, the greatest problem is to find a general method in three dimensions, that is able to obtain for any unperturbed Hamiltonian H_0 action-angle coordinates $(\boldsymbol{J}, \boldsymbol{\theta})$ (see Eq. 3.1) and a scheme for perturbative calculations in the vicinity of the different types of resonances. Despite encouraging results (Kaasalainen 1994), we are still far from having an efficient and simple method.

Nonetheless, insights can be obtained from numerical experiments. In particular, Fourier analysis can provide a fast classification of orbits in a potential, to determine if they are trapped or not to resonances.

3.3.1 Fourier spectra

Several works in the literature treat the subject of orbital spectral analysis in great detail (e.g., Binney & Spergel 1982; Laskar 1993; Carpintero & Aguilar 1998). All methods have in common a procedure that consists in numerical integrating orbits in a potential and obtaining numerically the Fourier transform of the time series of the coordinates $\mathbf{x}_i(t_i)$. If the orbit is regular in a N_d-dimensional space, the motion is quasi-periodic i.e.,

$$\mathbf{x}(t) = \sum_{k=1}^{\infty} \mathbf{a}_k e^{i\chi_k t}, \tag{3.30}$$

where $\mathbf{a}_k$ are the complex amplitudes and χ_k are linear combinations of the $N_\mathrm{f} \leq N_\mathrm{d}$ fundamental frequencies $\boldsymbol{\chi}$, i.e., $\chi_k = \mathbf{n}_k \cdot \boldsymbol{\chi}$. The Fourier transform of a quasi-periodic

signal like Eq. (3.30) is a sum of delta functions with amplitudes given by the coefficients $\mathbf{a}_k$. The delta functions become spikes of a certain width in the computation of the Fourier transform, as the resolution of the orbital integration $\Delta t = t_{i+1} - t_i$ is finite.

In the rest of this Chapter we consider orbits in configuration space (i.e., in 3D), described by the cylindrical coordinates (R, ϕ, z). First we integrate the orbits in a potential that resembles that of the Milky Way, for a time t_f and with resolution Δt (see details below), to obtain the time series $\mathbf{x}_i = (R_i, \phi_i, z_i)$. Then we derive the power spectrum $P_\xi(\omega_j)$ as

$$P_\xi(\chi_j) = \sqrt{\frac{1}{N}\left[\left(\sum_{i=1}^{N} \xi_i \cos \chi_j t_i\right)^2 + \left(\sum_{i=1}^{N} \xi_i \sin \chi_j t_i\right)^2\right]}, \tag{3.31}$$

where ξ is R or z and N is the number of time intervals. From this spectrum we select the frequency ω_ξ, where $P_\xi(\omega_\xi) = \max_j [P_\xi(\chi_j)]$, which is the frequency of the component of the motion with the highest amplitude. The frequency ω_ϕ is instead obtained as the slope of the straight line that gives the best fit to the points $(t_i, \phi_i + 2\pi N_\phi)$, where N_ϕ is the number of revolutions of the particle around the center of the potential (Athanassoula 2002; Ceverino & Klypin 2007).

3.3.2 Frequency maps

For each orbit the Fourier analysis gives a triad of frequencies $(\omega_R, \omega_\phi, \omega_z)$. In Fig. 3.3 we show a "frequency map". Here each point corresponds to an orbit characterized by $(\omega_R/\omega_z, \omega_\phi/\omega_z)$ (Binney & Tremaine 2008). This map was obtained for thin disk particles taken from the simulations described in Chapter 2, for the GB2 potential, in a cylindrical volume centered at $(R, \phi, z) = (8\ \mathrm{kpc}, -20°, 0)$ of width 300 pc and height 600 pc, in the final output of the simulation. To compute the frequencies we used $t_\mathrm{f} = 100T$, where $T = 2\pi \times (220/8\ \mathrm{km\ s^{-1}\ kpc^{-1}})^{-1}$ (approximately one dynamical time at the Sun's position in the Galaxy).

As we see, the dots are not uniformly distributed in the map, but they often group along straight lines. The orbits on lines in a frequency map are trapped to the same resonance. The colors correspond to the different resonances as given in Table 3.1.

To explain why orbits trapped to a resonances occupy lines in the frequency map, we use as an example a horizontal resonance $\Omega_R : \Omega_\phi = n : m$ ignoring the vertical motion, and therefore restricting the problem to 2D (similar considerations can be applied to the 3D case, and to the vertical resonances). When we apply the frequency analysis to the azimuth ϕ of the orbit, we fit a straight line to the curve (see Sect. 3.3.1)

$$\phi'(t) \equiv \phi(t) - \Omega_\mathrm{b} t = \theta_\phi(t) - \Omega_\mathrm{b} t - f(\theta_R(t)). \tag{3.32}$$

In an axisymmetric potential the $\theta_\phi(t) - \Omega_\mathrm{b} t$ part of the curve would correspond to a straight line, with periodic wiggles superposed to it, due to the $f(\theta_R(t))$ term (this is because ϕ is not a canonical angle, unlike θ_ϕ, and so does not vary as $\Omega_\phi t$). Therefore the frequency analysis would return the slope of $\theta_\phi(t) - \Omega_\mathrm{b} t$, i.e. $\Omega_\phi - \Omega_\mathrm{b}$. However, in the non-axisymmetric case the curve $\theta_\phi(t) - \Omega_\mathrm{b} t$ in general is not a straight line. In fact, we can rewrite it as

$$\theta_\phi(t) - \Omega_\mathrm{b} t = \frac{\phi_\mathrm{s}(t)}{l_\phi} - \frac{l_R}{l_\phi}\theta_R(t). \tag{3.33}$$

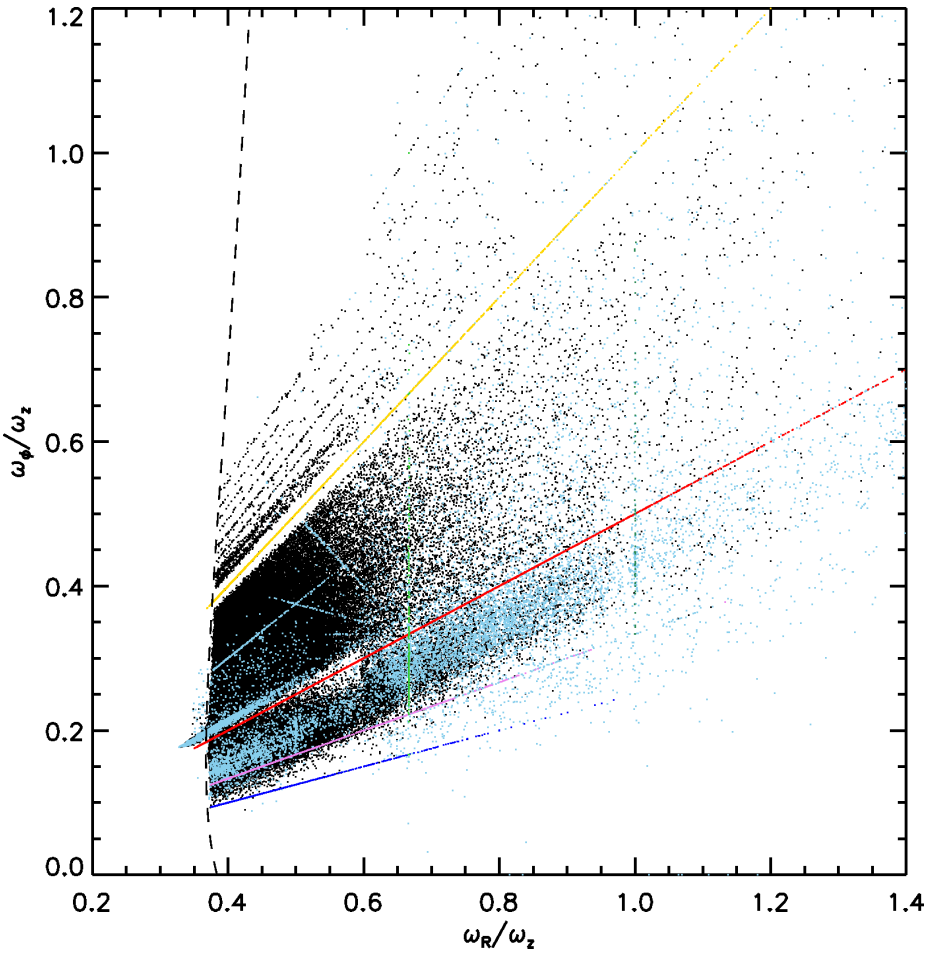

Figure 3.3: Frequency map for the particles inside a small cylinder of width 300 pc and height 600 pc, centered at $(R, \phi, z) = (8 \text{ kpc}, -20°, 0)$, for particles in the thin disk of the GB2 simulation presented in Chapter 2.

For an orbit trapped to a resonance $\Omega_\mathrm{s} \ll \Omega_R$, and so $\theta_\phi(t) - \Omega_\mathrm{b} t$ will also be a straight line perturbed by wiggles due to the precession of the orbit, where $\phi_\mathrm{s}(t)/l_\phi$, will librate between two values. In that case, the slope of the fitted straight line (i.e., the result of the frequency analysis) is due only to the second term in Eq. (3.33):

$$\omega_\phi = -\frac{l_R}{l_\phi}\Omega_R. \tag{3.34}$$

The $R(t)$ variable is a composition of a dominant component of the motion at a constant frequency Ω_R plus the periodic elongations due to the bar and dependent on $\phi_\mathrm{s}(t)$ (which follows from the lines of reasoning that led to Eq. (3.29)). The Fourier analysis will return the frequency of the motion with largest amplitude, i.e.,

$$\omega_R = \Omega_R. \tag{3.35}$$

Therefore the ratio

$$\frac{\omega_R}{\omega_\phi} = -\frac{l_\phi}{l_R}, \tag{3.36}$$

is a line in the frequency map. Conversely, an orbit not trapped to a resonance ϕ_s is circulating and contributes to the fit of the curve Eq. (3.33), so that the orbits do not line up in the frequency map anymore.

For orbits with low eccentricity and vertical amplitude $(\Omega_R, \Omega_\phi, \Omega_z) \approx (\kappa, \Omega - \Omega_\mathrm{b}, \nu)$. The parametric curve $(\kappa/\nu, [\Omega - \Omega_\mathrm{b}]/\nu)\,(R_\mathrm{g})$ is shown by the dashed line in Fig. 3.3, and represents the locus of orbits that would follow exactly the epicyclic approximation (here obtained using the $m = 0$ component of the Fourier decomposition of the potential in ϕ).

The lines in Fig. 3.3 suggest the way to identify the orbits trapped to the resonances. In what follows, we call orbits trapped to a resonance (l_R, l_ϕ, l_z) *regular* orbits with $|l_R\omega_R + l_\phi\omega_\phi + l_z\omega_z| < 0.001$. Notice that often the resonant orbits are defined as the ratio of frequencies, e.g., for $(l_R, l_\phi, l_z) = (1, 2, 0)$, $\omega_\phi/\omega_R = -l_R/l_\phi$.

3.3.3 Diffusion coefficients

Not all orbits in the potential considered will be regular (i.e., have sufficient integrals of motion to be restricted to a 3D torus in the phase-space). To characterize the regularity of an orbit (i.e., if an orbit can be written as Eq. (3.30), see also Binney & Tremaine 2008; Fux 2001) we define the diffusion coefficients. These are estimated as $d = |(\omega_1 - \omega_2)/\omega_1|$, where ω_1 and ω_2 are the frequency estimates derived in two intervals: for $t \in [0, 100T]$ and for $t \in [100T, 200T]$ respectively. The larger d, the more irregular is the orbit. We fix the threshold between regular and irregular orbits at $d_\mathrm{max} = 10^{-3}$ (Vasiliev & Athanassoula 2012). The fraction and distribution of irregular orbits is not very dependent on the exact value of this threshold: for $d_\mathrm{max} = 10^{-2}$ the fraction of irregular orbits decreases by less than $\sim 2\%$, while for $d_\mathrm{max} = 10^{-4}$ this fraction increases by $\sim 6\%$. In what follows, except for the computation of d, we use the frequencies obtained in the interval $t \in [0, 100T]$.

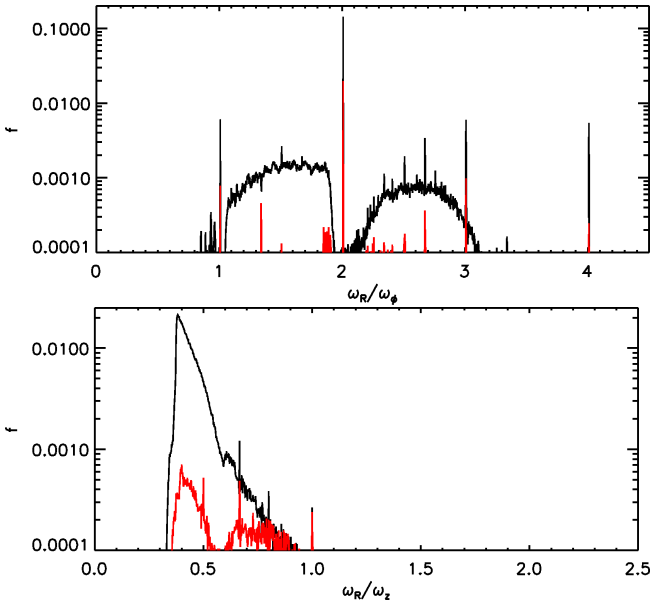

Figure 3.4: Distributions in the frequency ratios ω_R/ω_ϕ (top) and ω_R/ω_z (bottom) for the same volume of Fig. 3.3 for thin disk particles in our default bar simulation. In black we plot the regular orbits, in red those that are irregular.

3.4 Results

3.4.1 Distribution of frequencies

In Fig. 3.4 we show the fraction of particles (relative to the total number of particles in the volume) from the thin disk of the GB2 simulation (corresponding to our default bar model) of Chapter 2, as a function of ω_R/ω_ϕ (top) and ω_R/ω_z (bottom). The volume is a cylinder of width 300 pc and 600 pc height centered at $(R, \phi, z) = (8 \text{ kpc}, -20°, 0)$. This figure helps us to quantify the amount of resonant trapping in this potential and for this distribution of particles. We see that there are thin spikes present in the distributions, which correspond to the lines in Fig. 3.3. The most populated resonance is by far $(1, 2, 0)$, for almost $\sim 15\%$ of orbits are trapped to this resonance, followed by some much smaller spikes, e.g., $(1, 1, 0)$, $(1, 3, 0)$, $(1, 4, 0)$. The $R - z$ vertical resonances are very weakly populated, with only the $(3, 0, 2)$ resonance trapping $\sim 0.1\%$ of the orbits. The red curves in Fig. 3.4 represent the distribution of irregular orbits in the same volume. There is a peak of irregular orbits in the vicinity of $(1, 0, 2)$, $(1, 0, 1)$ and all the other resonances are populated by regular orbits. We can relate this to the fact that irregular orbits live in the surroundings of resonances.

In Fig. 3.5 we plot the distribution of frequencies but now for the thick disk. In this case the fraction of trapped orbits associated to horizontal resonances is slightly larger (especially for the $(1, 1, 0)$ resonance), and much larger in the vertical resonances

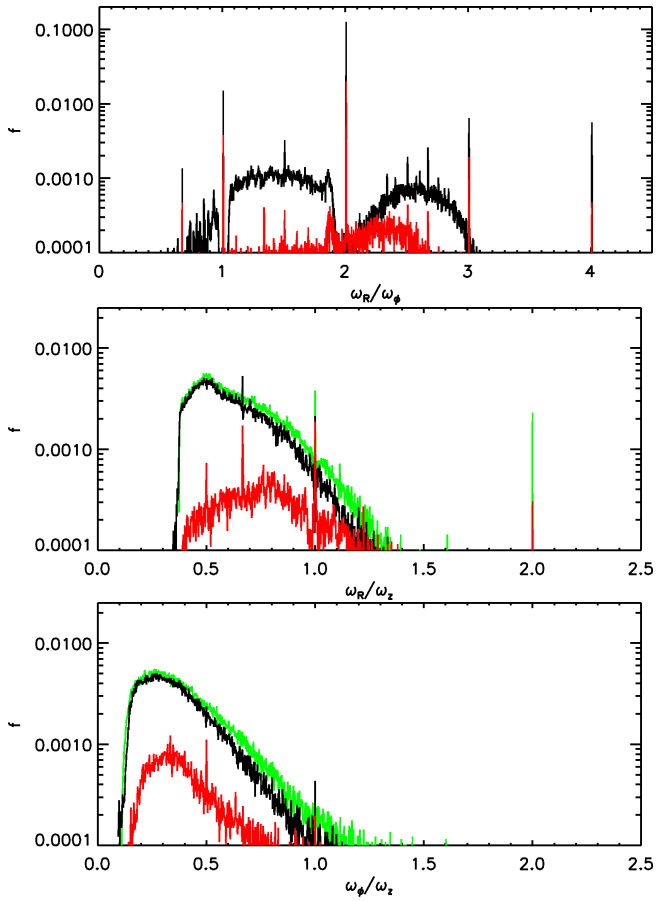

Figure 3.5: As in Fig. 3.4, but for the thick disk. We also include the distribution of the frequency ratios ω_ϕ/ω_z (bottom plot). The green line represents the frequencies for orbits computed in the axisymmetric potential A0+B2 (see Chapter 2).

Table 3.2: Fraction of orbits trapped to the main resonances inside a cylinder of width 300 pc and height 600 pc, centered at $(R, \phi, z) = (8 \text{ kpc}, -20°, 0)$, for thin and thick disk in the GB2 simulations from Chapter 2.

(l_R, l_ϕ, l_z)	Thin disk	Thick disk
$(1, 1, 0)$	0.6%	1.5%
$(1, 2, 0)$	14.2%	12.5%
$(1, 3, 0)$	0.6%	0.6%
$(1, 4, 0)$	0.5%	0.6%
$(3, 0, 2)$	0.1%	0.5%
$(1, 0, 1)$	0	0.2%
$(1, 0, 2)$	0	0.1%
Trapped	16%	16%
Irregular	6.4%	16.4%

($(3, 0, 2)$, $(1, 0, 1)$, $(1, 0, 2)$). Also the fraction of irregular orbits is larger. For comparison we have also computed the fraction of orbits trapped to vertical resonances, for the axisymmetric potential used in the simulations of Chapter 2 before the growth of the bar using as initial conditions the positions and velocities of the particles in the thick disk of the GB2 simulations at the final time[2]. Interestingly, the green curve shows how trapping to the $R - z$ vertical resonances is already present in the axisymmetric part of potential[3] and is therefore not induced by the bar. Therefore, the only vertical frequencies genuinely related to the bar are those between the $\phi - z$ coordinates (or between $R - \phi - z$), that are represented in the bottom plot of Fig. 3.5. Some of the $\phi - z$ are present (e.g., $(0, 1, 1)$), however the fraction of orbits trapped to these resonances is negligible ($< 0.1\%$). Table 3.2 summarizes the fraction of trapped and irregular orbits in this volume both for the thin and the thick disks.

3.4.2 Frequencies and velocity distributions

In Fig. 3.6 we show the (v_R, v_ϕ) velocity distribution of the particles in the same volume considered in the previous Section (left panel: thin disk, right panel: thick disk). The color coding corresponds to the trapping to the main resonances as given in Table 3.1.

The left panel of Fig. 3.6 shows that the orbits trapped to $(1, 2, 0)$ are localized in v_R vs. v_ϕ, and that they define a horn-like feature. This horn-like feature of the v_R vs. v_ϕ distributions was already described in Chapter 2 and is present also in the simulations of e.g., Dehnen (2000) and Fux (2001). The location of this feature corresponds well to the $(1, 2)$ resonance computed using the perturbation analysis of Sect. 3.2.2, as shown in top left panel of Fig. 3.2. It seems, therefore, that the expectations of the perturbation theory are also valid for these 3D simulations, although of course the details are different.

[2] We obtain similar results performing the analysis for particles in the axisymmetric initial conditions for the same volumes.

[3] In fact, resonant trapping and irregular orbits can exist also in realistic galactic axisymmetric potentials, even though such orbits occupy a small region of the phase-space (Henon & Heiles 1964).

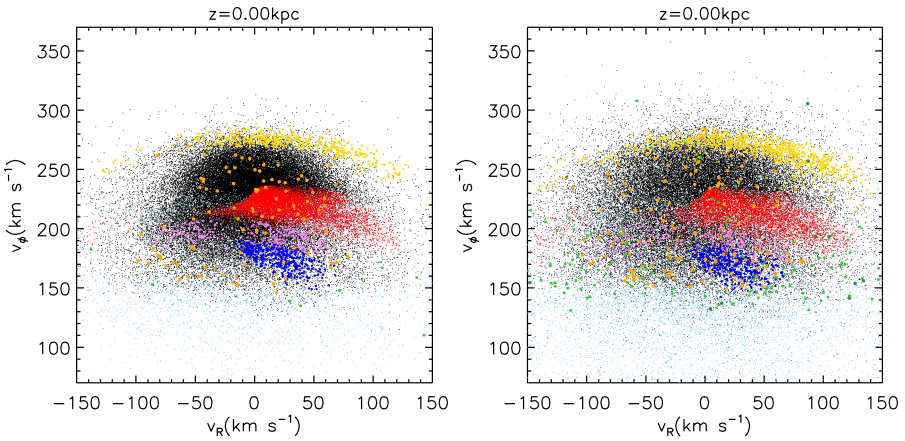

Figure 3.6: v_R vs. v_ϕ distributions of a random subsample of 50000 particles from the same volume as in Fig. 3.3, color coded with the orbits trapped to the resonances, for thin (left) and thick disk (right) particles.

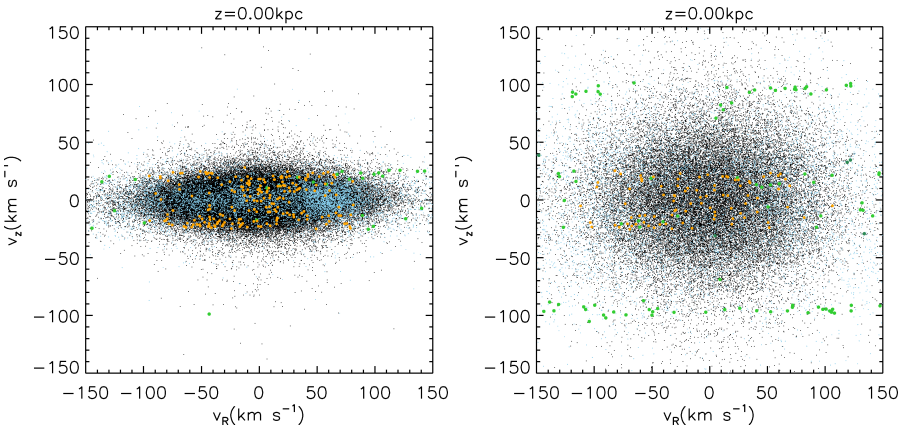

Figure 3.7: v_R vs. v_z distributions of a random subsample of 50000 particles from the same volume as in Fig. 3.3, color coded with the orbits trapped to the resonances, for thin (left) and thick disk (right) particles. In this case we only show the two most populated vertical resonances: the dark green points correspond to $(1, 0, 1)$ and the orange points to $(1, 0, 2)$.

As in Fig. 3.2, we notice that for $v_R < 0$ there is almost complete depletion of $(1, 2, 0)$ orbits. The orbits trapped to $(1, 1, 0)$ and $(1, 3, 0)$ are localized both at positive and negative v_R as also seen in Fig. 3.2. Only $(1, 4, 0)$ seems to be distributed differently in our simulations as it is only found for $v_R > 0$ while in Fig. 3.2 it can be seen both in $v_R > 0$ and $v_R < 0$.

The right panel of Fig. 3.6 shows that the distribution in the v_R vs. v_ϕ space for particles in the thick disk associated to trapped orbits is similar. The only difference is that all the resonances are more populated, especially those in the tails of the velocity distribution, such as $(1, 1, 0)$.

Both for the thin and thick disks the irregular orbits are distributed in wide regions, but they are mostly concentrated near to trapped orbits. This is especially clear in the valley formed by the $(1, 2, 0)$ resonance at $v_\phi \sim 200$ km s^{-1} (see Chapter 2). This is expected, as irregular orbits occupy in phase-space the gaps between regions of resonant trapping, as commonly observed using Surfaces of Section methods (Binney & Tremaine 2008).

Finally, in Fig. 3.7 we plot the v_R vs. v_z distribution. This time, however, we highlight only the orbits trapped to the vertical resonances, as the horizontal resonances are evenly distributed in v_z. We see how the stars on orbits trapped to $(1, 0, 1)$ (green dots) tend to be distributed at high $|v_z|$, both for the thin and the thick disk. The density of this kind of orbits is in fact larger farther away from the disk plane (see below), and so only orbits with large v_z reach these heights. However, in small volumes centered at $z = 0$, the fraction of orbits trapped to the vertical resonances is almost negligible. Also apparent from Fig. 3.7 is that the v_z distribution is smooth and so the resonant orbits do not lead to the appearance of features in the vertical velocity distribution.

3.4.3 Distribution of guiding centers

In Fig. 3.8 we have plotted the v_R vs. v_ϕ velocity distribution for thin disk particles in a volume centered at $(R, \phi, z) = (8 \text{ kpc}, -20°, 0)$ from the GB2 simulation of Chapter 2, color coded by the location of their guiding center radius. The red points have $R_\text{g} < R_\text{OLR}$, the blue points have $R_\text{g} > R_\text{OLR}$. Our proxy for R_g is the average R of the orbits computed over the same time interval used to derive the frequencies.

This plot shows that the guiding centers of the orbits almost perfectly trace the bimodality in the velocity distribution induced by the bar. The OLR Mode (see Chapter 2) is composed by particles with $R_\text{g} < R_\text{OLR}$, i.e., stretched perpendicular to the bar and the LSR Mode by orbits with $R_\text{g} > R_\text{OLR}$, stretched parallel to the bar, as shown in the top panels of Fig. 3.1.

The orbits with $R_\text{g} < R_\text{OLR}$ have a net outward motion and those with $R_\text{g} > R_\text{OLR}$ an inward motion, from which the bimodality in the velocity distribution results, as in Kalnajs (1991) hypothesis. The analysis of the thick disk particles in the same volume leads to similar conclusions.

3.4.4 Trends as a function of z

In Fig. 3.9 we show the fraction of orbits trapped to the different resonances as a function of z, inside a cylinder of width 300 pc and height 4 kpc, centered at $(R, \phi, z) = (8 \text{ kpc}, -20°, 0)$, for the thin (top panel) and thick disk (bottom panel). From these

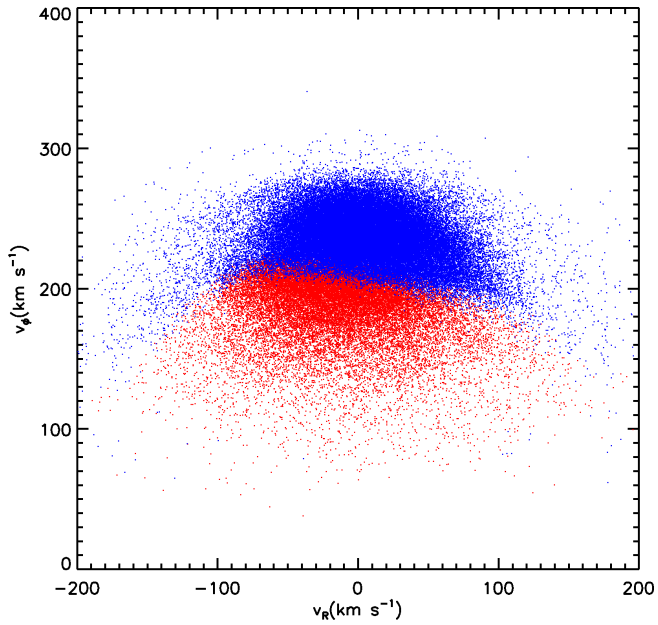

Figure 3.8: Velocity distribution of the particles inside a cylinder of width 300 pc and height 600 pc, centered at $(R, \phi, z) = (8 \text{ kpc}, -20°, 0)$, for the thin disk simulation GB2, from Chapter 2. Here the red dots have guiding center radii $R_g < R_{OLR}$, while the blue dots have $R_g > R_{OLR}$.

figures we see that the fraction of orbits trapped to horizontal $R-\phi$ resonances is almost constant with distance from the disk plane in the wide range of z considered ($|z| < 2$ kpc), both for the thin and thick disk. Therefore the *amount* of horizontal trapping seems to be independent on z. This is in agreement with the results of Chapter 2, where we noticed that the total effect of the bar on the horizontal velocity distribution induced by the bar to be nearly independent of z. The fraction of orbits trapped to vertical resonances instead increases with z (orange, green and gray line) for all the vertical resonances that we considered. However, the fraction of particles trapped to those resonances genuinely induced by the bar (e.g., $(0, 1, 1)$, gray line) always remains very moderate in magnitude. The resonance that seems to be most populated is $(1, 0, 1)$ (green line) for the thick disk. In particular at ~ 2.5 kpc (outside of the axes range of the plot) the amount of particles trapped to this resonance is non-negligible ($\sim 8\%$). However there is no clear sign of a kinematical effect of this resonance on the velocity distribution for thick disk particles at these heights. The fraction of irregular orbits also slightly increases with z, as the vertical resonances become more populated.

In Figs. 3.10 and 3.11 we study how the characteristic parameters of the velocity distribution of the particles associated to the various resonant families changes with height from the Galactic plane. These figures plot the average of each of the three velocity components for particles inside the same bins as in Fig. 3.9. We see how the

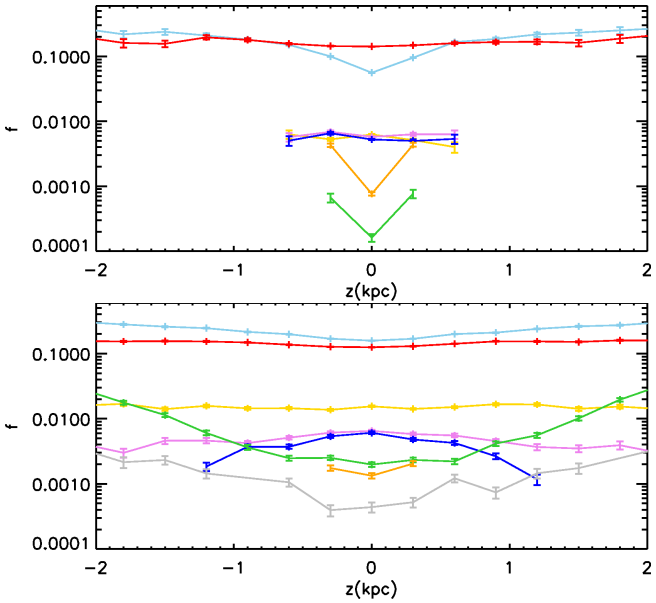

Figure 3.9: Fraction of trapped orbits as a function of the distance from the disk plane z, for particles in the GB2 simulation, inside a cylinder of width 300 pc centered at $(R, \phi, z) = (8 \text{ kpc}, -20°, 0)$ and height 4 kpc. These curves are made using independent vertical bins of size 300 pc. The error bars on the averages are due to the Poisson noise associated to the finite number of particles. Top: thin disk. Bottom: thick disk.

average v_R and v_z reflects what we saw in Sect. 3.4.2, namely that $\langle v_z \rangle = 0$ and $\langle v_R \rangle \neq 0$ for the different horizontal resonant families for $z = 0$, and how this behavior remains almost unchanged with z. The only exception seems to be a tendency for the orbits trapped to the $(1, 2, 0)$ and especially $(1, 1, 0)$ to have positive v_z for $z < 0$ and negative v_z for $z > 0$. The rotational velocity v_ϕ of the trapped orbits is instead clearly decreasing as $|z|$ increases. In fact, the v_ϕ position of the resonances varies following the change with z of the axisymmetric part of the potential $\Phi_0(R, z)$, while the potential of the bar is almost constant with z. Notice that a related manifestation is that $\langle v_\phi \rangle$ of the whole distribution (black lines) decreases with $|z|$ as expected from the asymmetric drift relation (Binney & Tremaine 2008).

3.4.5 Trends as a function of ϕ

In Fig. 3.12 we show the trend in the fraction of trapped orbits and in their average velocity as a function of the angle from the long axis of the bar ϕ, for orbits in the thin disk of the GB2 simulation, in an annulus of 600 pc width and 600 pc height, centered at $R = 8$ kpc and $z = 0$. From this figure we see that the fraction of orbits trapped to the resonances is a periodic function ϕ, and the same is true for the average horizontal velocity v_R and v_ϕ components. Notice how the periodicity depends on the geometry of

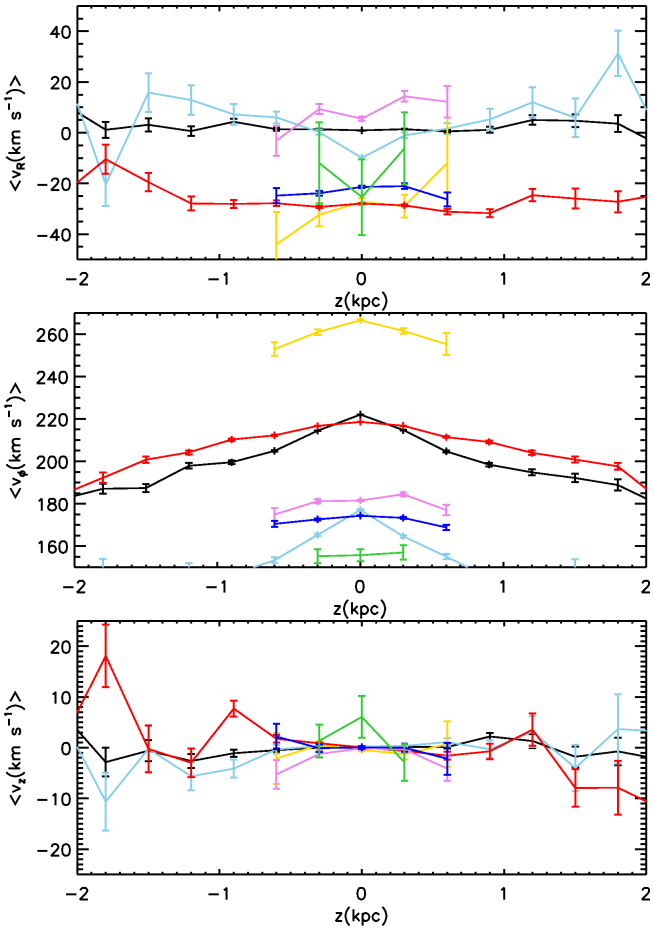

Figure 3.10: Average velocities inside independent vertical bins of size 300 pc for the thin disk in GB2. The different colors correspond to orbits trapped to different resonances (e.g., $(1, 2, 0)$, red line), the irregular orbits (light blue line) and all the particles (black line). The detailed color scheme is given in Table 3.1.

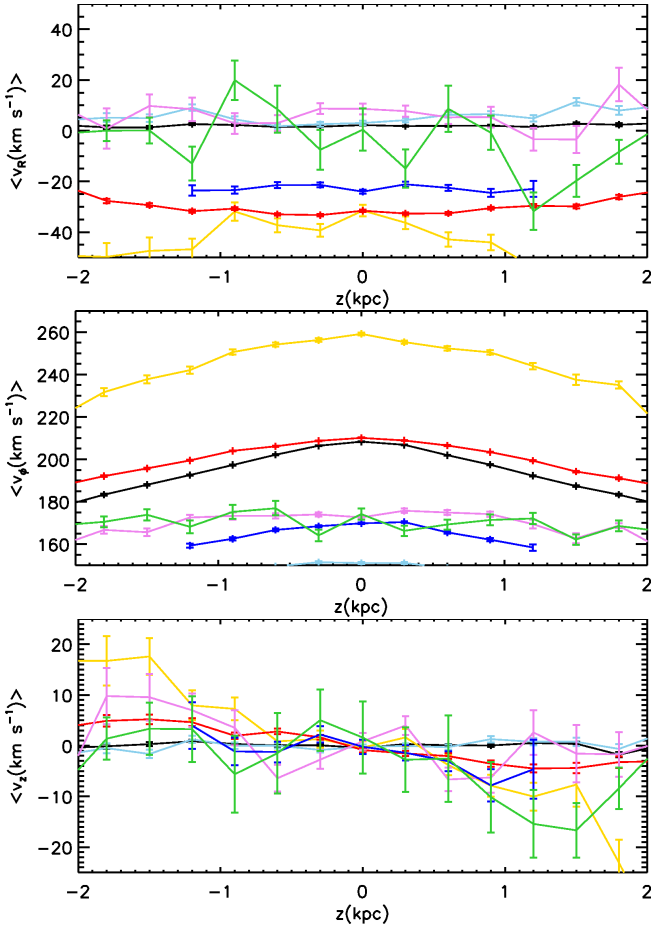

Figure 3.11: As in Fig. 3.10, but for the thick disk.

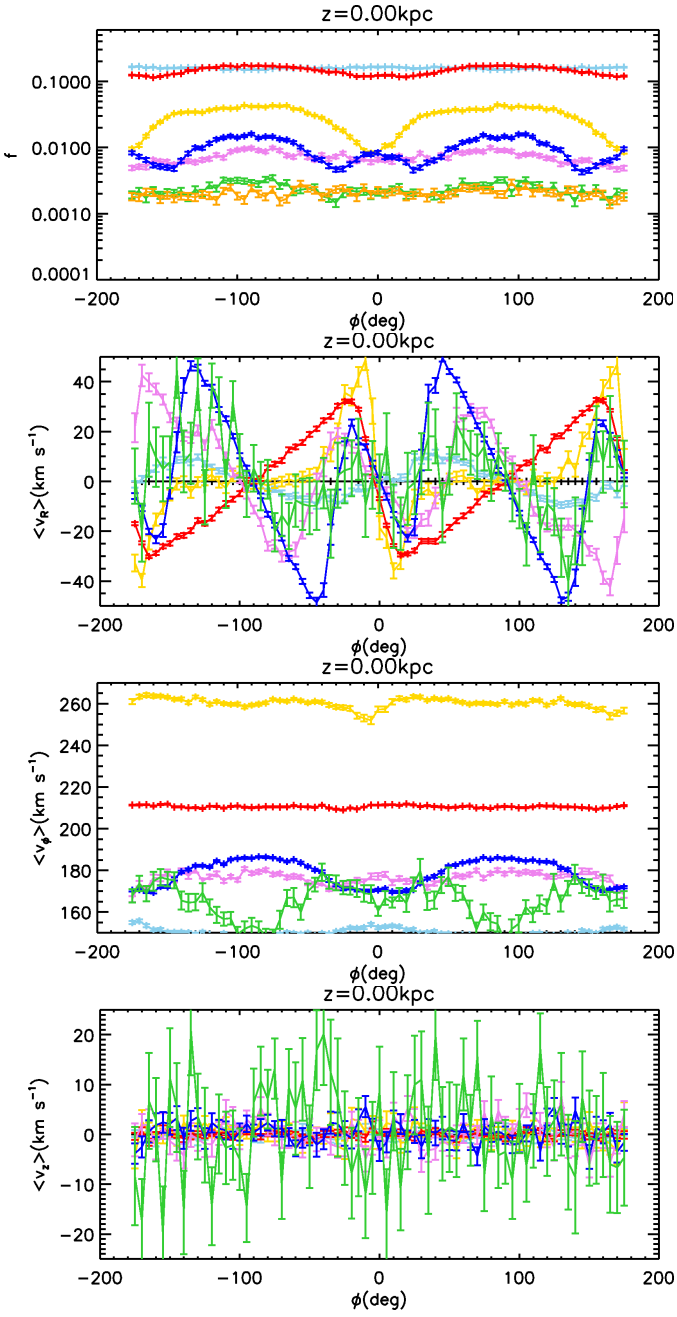

Figure 3.12: Fraction of trapped orbits and average velocities as a function of ϕ, for thin disk particles in the GB2 simulation, inside a ring of 600 pc radial extent and height 600 pc, centered at $R = 8$ kpc and $z = 0$. The error bars represent the Poisson noise. Only those bins with more than 25 particles are shown.

the type of orbits considered. For example, it is very clear that the $\langle v_R \rangle$ of the $(1,2,0)$ orbits oscillates twice in the ϕ range $[-180°, 180,°]$, while the $\langle v_R \rangle$ of $(1,4,0)$ oscillates four times. Moreover, the amplitude of the oscillation changes with ϕ because the bar stretches the same orbits parallel and perpendicular to its long axis[4]. These results seem to agree with the predictions from the perturbation theory in 2D, that show that the angle ϕ mostly influences the v_R position of the orbits trapped to the resonances, with different periodicity depending on the different resonances. It is also interesting to notice how the orbits trapped to the vertical resonance $(1,0,1)$ have oscillations in the horizontal velocities, and that $\langle v_z \rangle$ does not depend at all on ϕ.

The behavior with ϕ of the trapped orbits of the thick disk, both on and far from the plane, is qualitatively similar to what was just discussed for the thin disk.

3.4.6 Trends as a function of R

In Fig. 3.13 we plot the average velocity of the various resonant families as well as their fraction as function of distance R from the Galactic center for $R \in [6.5, 9.5]$ kpc. Here we consider the GB2 simulation for volumes centered at $\phi = -20°$, $z = 0$. The trends in the thick disk are very similar. The velocity trends that we find are consistent with the expectations from the perturbation analysis. In particular the $\langle v_\phi \rangle$ of the horizontal resonances always decreases going outwards in the Galaxy. Inside (outside) the Outer Lindblad Resonance, at $R = 7.69$ kpc, $\langle v_R \rangle$ of the $(1,2,0)$ orbits is decreasing (increasing). At the same time $\langle v_z \rangle \sim 0$ for all the cases we consider. The fraction of trapped orbits increases or decreases with R as we are approaching (e.g., for $(1,1,0)$, $(1,2,0)$) or leaving the position of a resonance in the Galaxy (as in the case of $(1,3,0)$, $(1,4,0)$). Interestingly, the peak of orbits trapped to $(1,2,0)$ does not occur precisely at the Outer Lindblad Resonance, but rather at $R \sim 8.5$ kpc.

3.4.7 Other bar models

In this section we present the results of the frequency analysis for two other bar models. We select the GB1 and LB2 bar models from Chapter 2. The GB1 model corresponds to the less massive bar and has the same geometry of the GB2 model discussed so far. The LB2 has the same mass but a different geometry from GB2 (see Chapter 2 for more details).

We focus here on the fraction of orbits trapped to the resonances for these models, as we expect to see the most interesting differences or similarities for this quantity.

In Fig. 3.14 (top) we show the fraction of orbits trapped to the resonances for the GB1 model, for a cylindrical volume of width 300 pc centered at $(R, \phi) = (8 \text{ kpc}, -20°, 0)$, in the thick disk case. In this case we plot all bins containing at least 4 particles. This plot should be compared to the bottom panel of Fig. 3.9 for GB2.

The main difference is that the fraction of orbits trapped to the resonances or irregular orbits is lower in GB1 than in GB2. For example, the fraction of orbits trapped to $(1,2,0)$ is 9% and the fraction of irregular orbits is 12% in the bin centered at $z = 0$, compared to 12% and 16% for GB2. This is a consequence of the fact that the bar mass in GB1 is smaller (by a factor of 2) and therefore the perturbation on the axisymmetric part of the

[4] A second reason for some of the variation with ϕ is that the simulation is not completely phase-mixed (see Sect. 2.3.2 of Chapter 2).

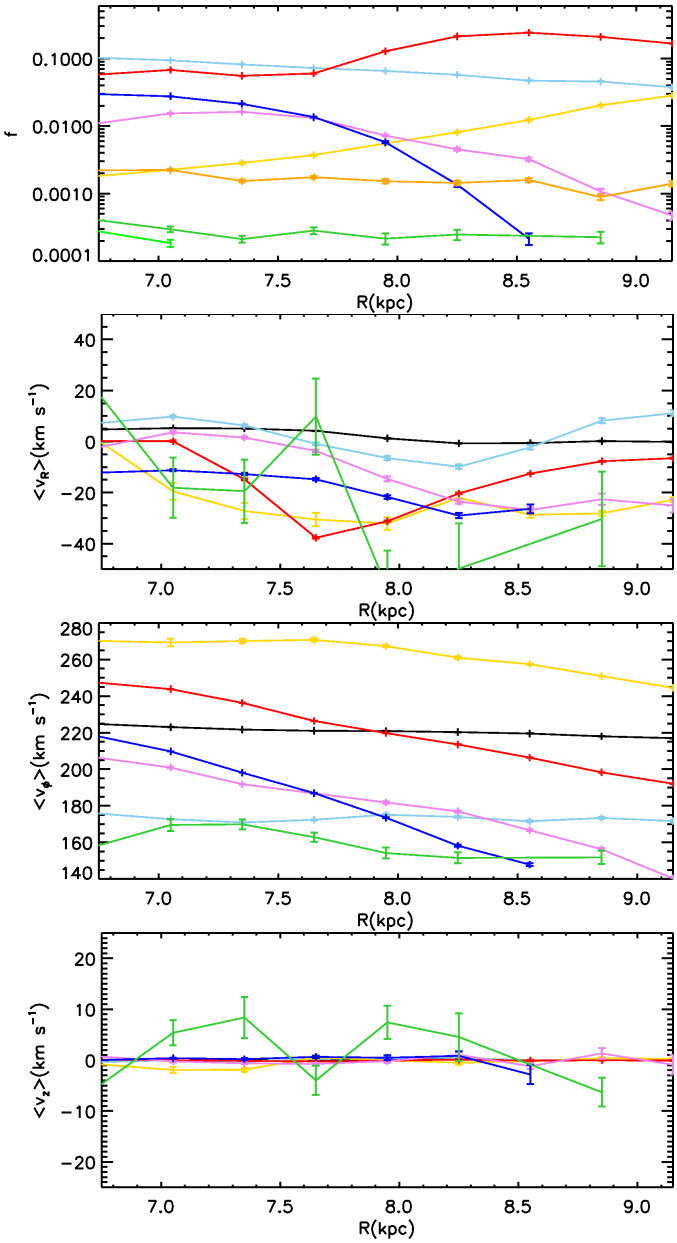

Figure 3.13: Fraction of trapped orbits and average velocities as a function of R, for particles of the thin disk in the GB2 simulation, inside volumes aligned at $\phi = -20°$ and $z = 0$. The errors bars represent the Poisson noise. Only those bins with more than 25 particles are shown.

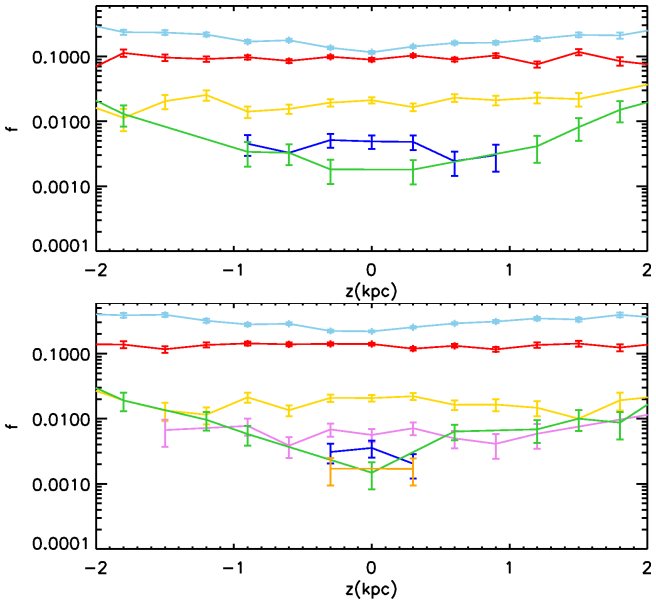

Figure 3.14: As in Fig. 3.9, for the GB1 model (top) and LB2 (bottom), for the thick disk. The error bars represent the Poisson noise of the fraction. In this case only those bins where the fraction is twice as big as the error are shown.

potential is also lower, which results in a smaller fraction of the phase-space occupied by resonant trapping or irregular orbits, as we saw also in the perturbation analysis of Sect. 3.2, and specifically in Fig. 3.2.

Note that as in the GB2 case, the fraction of trapped orbits remain constant with z for the horizontal resonances and increases with z for the vertical resonances (in green and orange).

The LB2 case is shown in the bottom panel of Fig. 3.14. Even if in this case the only difference from GB2 is the geometry of the bar, as we have explained in Chapter 2 the net effect in the Solar Neighborhood is a larger perturbation to the axisymmetric part of the potential.

As a consequence, the fraction of orbits trapped to the resonances is larger in LB2, with 14% of orbits trapped to $(1, 2, 0)$ and 22% of irregular orbits. As before the fraction of orbits trapped to horizontal resonances, stays constant with z, like all the other bar models that we explored here, despite the fact that the LB2 bar is flatter that in GB2.

3.5 Summary and conclusions

We have studied the dynamical characteristics of disk stars in a galactic potential resembling that of the Milky Way, and which includes a bar, halo and thin and thick disks. Our interest is in the effects of the bar on the kinematics of stars, in particular

close to the Sun, but also as function of location across the disk (i.e., distance from the Galactic center and angle from the major axis of the bar). To this end, we have used the simulations presented in Chapter 2, and shifted our focus to the characterization of the resonances induced by the bar and their relation to the kinematical features found earlier in this Thesis.

In the case of the Milky Way, as well as in our simulations, the bar can be seen as a perturbation on a background axisymmetric potential. This has allowed us to model the dynamics of stars using a perturbation analysis in 2D along the lines of Weinberg (1994). In this way we have identified orbital families that are trapped to resonances. We have then established how these trapped orbits map onto velocity space, especially for stars in the vicinity of the Sun, and found that they define "islands" in (v_R, v_ϕ) velocity space. Furthermore, we have shown that the $\langle v_R \rangle$ velocity of the trapped orbits depends on the angle from the bar and the $\langle v_\phi \rangle$ velocity depends on the distance from the center of the Galaxy and the type of resonance. Moreover, the stronger the bar force, the larger the regions of resonant trapping in the velocity space.

Since the simulations presented in Chapter 2 are 3D, the gravitational potential is somewhat more complex, and the stars follow specific distributions (both spatially and kinematically), we have performed a Fourier frequency analysis to study the resonant trapping present in those simulations. This analysis shows that an important fraction of the orbits ($\sim 16\%$) is trapped to the resonances in a solar neighborhood volume. The most populated resonance is the $(1, 2, 0)$ ($\Omega_R : \Omega_\phi = 2 : 1$), with $\sim 14\%$ trapped and defining a distinct feature in the velocity distribution. The remaining resonances are less populated, and $\sim 6\%$ of the stars in this volume are on irregular orbits.

Interestingly, we have found that the fraction of orbits trapped to horizontal resonances ($\Omega_R : \Omega_\phi$) does not depend on distance from the disk plane z. This is consistent with the analysis of the (v_R, v_ϕ) velocity distribution as function of height z, where characteristic features, which we can now directly associate to orbital trapping, are present at all heights explored.

On the other hand, the fraction of orbits trapped to the vertical resonances does increase with z. However, the vertical resonances do not influence significantly the velocity distribution, as they do not define specific features in velocity space.

More generally, we have also found that the fraction of trapped orbits and their location in velocity space varies mostly with R and ϕ position in the Galaxy, while the effect of z is mostly to shift $\langle v_\phi \rangle$ of the trapped orbits.

Finally we have also explored two other bar models (a bar with half of the mass than the default bar discussed in the rest of the Chapter but with the same geometry, and a bar with different geometry but the same mass). The main difference between the models lies in the number of trapped and irregular orbits, that depends on the strength of the perturbation. In particular, for our less massive bar model these fractions are smaller and for our long bar model are larger than in our default model.

Acknowledgements

We would like to thank E. Vasiliev for useful discussions. The authors gratefully acknowledge support from the European Research Council under ERC Starting Grant GALACTICA-240271.